Available online at www.sciencedirect.com
ScienceDirect
International Journal of Heat and Fluid Flow 27 (2006) 852–866
International Journal of HEAT AND FLUID FLOW
www.elsevier.com/locate/ijhff

An analytical wall-function for turbulent flows and heat transfer over rough walls

K. Suga [a,*], T.J. Craft [b], H. Iacovides [b]

[a] Computational Physics Lab., Toyota Central R&D Labs., Inc., Nagakute, Aichi 480-1192, Japan
[b] School of Mechanical, Aerospace and Civil Engineering, The University of Manchester, P.O. Box 88, Manchester M60 1QD, UK

Received 10 September 2005; received in revised form 6 December 2005; accepted 4 March 2006
Available online 15 June 2006

Abstract

This paper reports the development of a refined wall-function strategy for the modelling of turbulent forced convection heat transfer over smooth and rough surfaces. In order to include the effects of fine-grain surface roughness, the present study extends a more fundamental work by Craft et al. [Craft, T.J., Gerasimov, A.V., Iacovides, H., Launder, B.E., 2002. Progress in the generalisation of wall-function treatment. Int. J. Heat Fluid Flow 23, 148–160] on the development of advanced wall-functions of general applicability. The presently proposed model is validated through comparisons with data available for internal flows through channels and for external flows over flat and curved plates with both smooth and rough surfaces. Then, its further validation in separating flows over a sand dune and a sand-roughened ramp is discussed. The validation results suggest that the presently proposed form can be successfully applied to a wide range of attached and separated turbulent flows with heat transfer over smooth and fine-grain rough surfaces.

Keywords: Wall-function; Turbulence modelling; Rough wall; Heat transfer

1. Introduction

Although many recent low-Reynolds-number (LRN) turbulence models perform satisfactorily, industrial engineers still routinely make use of classical wall-function approaches for representing near-wall turbulence and heat transfer (e.g., Ahmed and Demoulin, 2002). One reason for this is that, despite advances in computing power, their near-wall resolution requirements make LRN models prohibitively expensive in complex three-dimensional industrial heat and fluid flows. This is particularly true for flows over rough surfaces, which are common in industrial applications. Since one cannot hope to resolve the details of small wall-roughness elements, the wall-function approach may be the only practical strategy for such industrial applications.

Despite the above comments, in contrast to many other modelling issues, not so many researchers focused on the wall-functions over the last few decades after the establishment of the "standard" log-law wall-function. The most part of the log-law wall-function strategies was proposed by the 1970s with the assumption of semi-logarithmic variations of the near-wall velocity and temperature (e.g., Launder and Spalding, 1974). Chieng and Launder (1980) improved the wall-function by allowing for a linear variation of both the shear stress and the turbulent kinetic energy across the near-wall cell. Johnson and Launder (1982) considered the variation of the viscous sub-layer thickness corresponding to the non-uniform shear stress variation near the wall. Amano (1984), Ciofallo and Collins (1989) and Grotjans and Menter (1998) also attempted to improve the wall-functions. However, all the above attempts were still based on the log-law and it is well known that such a condition does not apply in flows with

* Corresponding author. Present address: Department of Mechanical Engineering, Osaka Prefecture University, Sakai 599-8531, Japan, Tel.: +81 72 254 9224; fax: +81 72 254 9904.
E-mail address: suga@me.osakafu-u.ac.jp (K. Suga).

0142-727X/$ - see front matter © 2006 Elsevier Inc. All rights reserved.
doi:10.1016/j.ijheatfluidflow.2006.03.011

Nomenclature

A_T, A'_T, B_T, B'_T integration constants from the energy equation
A_U, A'_U, B_U, B'_U integration constants from the momentum equation
c_p specific heat capacity at constant pressure
c_ℓ, c_μ model constants
C_0 model coefficient
C_f friction coefficient
C_p pressure coefficient
C_T sum of the convection and the diffusion terms of the energy equation
C_U sum of the convection and the diffusion terms of the momentum equation
d diameter of hemispherical roughness element
D pipe diameter or channel height
f friction coefficient of pipe flows
h, h^* roughness height i equivalent sand grain roughness height: $h\sqrt{k_P}/\nu$
h^+ roughness Reynolds number: hU_τ/ν
H ramp height
k, k_P turbulence energy, k at node P
ℓ turbulent length scale
L spacing between hemispherical roughness elements or ramp length
Nu Nusselt number
P pressure or cell center of the wall-adjacent cell
P_k production term of k equation
Pr Prandtl number
Pr_t, Pr_t^∞ turbulent Prandtl numbers
q_w wall heat flux
Re, Re_x, Re_θ Reynolds numbers: $U_b D/\nu$, $U_0 x/\nu$, $U_e\theta/\nu$; θ: momentum thickness
St Stanton number: $Nu/(Re\,Pr)$
S_θ source term of the energy equation
U_b, U_τ bulk velocity, friction velocity
U_e, U_0 free stream velocities
U_n velocity at the point n
x wall parallel coordinate
x' x/L in the ramp flow
y wall normal coordinate or wall normal distance
y_n, y_v, y_ε cell height, viscous sub-layer thickness, characteristic dissipation length
y^+, y^* normalized distances: yU_τ/ν, $y\sqrt{k_P}/\nu$
Y^*, Y_i^* $1+\alpha(y^*-y_v^*)$, $1+\alpha(y_i^*-y_v^*)$; $i=w, n, h$; $y_w=0$; $y_h=h$
$Y^{\alpha T}, Y_i^{\alpha T}$ $1+\alpha_T(y^*-y_v^*)$, $1+\alpha_T(y_i^*-y_v^*)$; $i=w, n, h$; $y_w=0$; $y_h=h$
$Y^{\beta T}, Y_i^{\beta T}$ $1+\beta_T(y^*-y_v^*)$, $1+\beta_T(y_i^*-y_v^*)$; $i=w, n, h$; $y_w=0$; $y_h=h$
α $c_\mu c_\ell$ or heat transfer coefficient: $q_w/(\Theta_w-\Theta_{inlet})$; q_w: local wall heat flux
α_T, α_θ $\alpha Pr/Pr_t^\infty$, $\alpha Pr/Pr_t$
β_T $C_0/(h^* Pr_t^\infty)$
Δx, Δy cell widths in the x, y direction
ε dissipation rate of k
Θ, Θ^+ mean temperature, $|\Theta-\Theta_w|(\rho c_p U_\tau)/q_w$
Θ_w, Θ_n wall temperature, temperature at the point n
κ von Kármán constant: 0.42
λ_b $Y_w^{\alpha T}+\beta_T h^*$
μ, μ_t viscosity, turbulent viscosity
ν, ν_t kinematic viscosity, kinematic turbulent viscosity
ρ fluid density
τ_w wall shear stress

strong pressure gradients and separation (e.g., Launder, 1984, 1988). Moreover, since a universal scale for turbulent buoyant thermal boundary layers has not been established yet, it is difficult to use empirical wall-functions for such phenomena (Hanjalić, 2002).

For rough wall turbulence, there have been several attempts to replace the classical wall-function approach. In order to directly consider the effects of the shape, size and distribution of the roughness elements, Christoph and Pletcher (1983) and Taylor et al. (1985) modified the mixing-length model introducing the blockage effects of roughness array. This discrete element model, however, cannot be immediately applicable to sandgrain or similar roughness cases. Patel and Yoon (1995) tested the rough wall extensions of the k–ω and the two-layer k–ε models. Durbin et al. (2001) and Aupoix and Spalart (2003) respectively modified the two-layer k–ε model and a one-equation model. Although these extensions overcome some of the defects of the classical wall-function for rough walls, they instead require a fine grid resolution near the walls. In other words, they are LRN turbulence models extended for capturing rough wall effects and thus they are not categorised as wall-functions.

In order to address industrial requirements, several attempts for developing new wall-function approaches were made. Smith (1990) discussed a wall-function in which simplified boundary layer transport equations were solved numerically. This approach showed good performance in several boundary layer flows including transonic, supersonic and hypersonic flows. More recently, Shih et al. (2003) employed a combined velocity scale composed of a friction velocity and a pressure gradient. Although the logarithmic velocity distribution was still used, they obtained successful results for flows with a separation and an adverse pressure gradient according to the use of the combined velocity scale. The UMIST group also proposed two alternative wall-function strategies (Craft et al., 2002, 2004). While still semi-empirical in nature, the model by Craft et al. (2002) makes assumptions at a deeper, more general level than the log-law based schemes. This

approach is called the analytical wall-function (AWF) and integrates simplified mean flow and energy equations analytically over the control volumes adjacent to the wall, assuming a near-wall variation of the turbulent viscosity. (In the context of large eddy simulations, Cabot and Moin (1999) discussed a wall model whose basic idea was similar to that of the AWF, though it used an implicit formla of the wall shear stress.) The resulting analytical expressions then produce the value of the wall shear stress and other quantities which are required over the near-wall cell. (Another strategy by Craft et al., 2004 employs a subgrid based approach which requires numerical integration of boundary layer equations for near-walls.)

Following this strategy, the objectives of this study is to propose and validate an extension to the AWF approach that allows for the effects of fine-grain surface roughness. It will be shown that relatively simple adaptations of the method result in an approach that does reproduce many of the features of flows and forced convection heat transfer over rough surfaces, whilst retaining the computational efficiency associated with wall-functions. The flow test cases chosen for the validation are internal flows through rough pipes and channels, external flows over flat and curved rough surfaces and separating flows over a sand dune and a sand-roughened ramp.

2. Wall-function approach

Although the wall-function approach is well known, it may be useful to recall the main features of its implementation.

A simplified transport equation for ϕ near-walls:

$$\frac{\partial}{\partial x}(\rho U\phi) = \frac{\partial}{\partial y}\left(\Gamma\frac{\partial\phi}{\partial y}\right) + S_\phi \tag{1}$$

can be integrated using the finite volume method over the cells illustrated in Fig. 1 giving

$$\int_s^n\int_w^e \frac{\partial}{\partial x}(\rho U\phi)\,\mathrm{d}x\,\mathrm{d}y = \int_s^n\int_w^e \frac{\partial}{\partial y}\left(\Gamma\frac{\partial\phi}{\partial y}\right)\mathrm{d}x\,\mathrm{d}y + \int_s^n\int_w^e S_\phi\,\mathrm{d}x\,\mathrm{d}y, \tag{2}$$

$$[(\rho U\phi)_e - (\rho U\phi)_w]\Delta y = \left[\left(\Gamma\frac{\mathrm{d}\phi}{\mathrm{d}y}\right)_n - \left(\Gamma\frac{\mathrm{d}\phi}{\mathrm{d}y}\right)_s\right]\Delta x + \overline{S_\phi}\,\Delta x\,\Delta y, \tag{3}$$

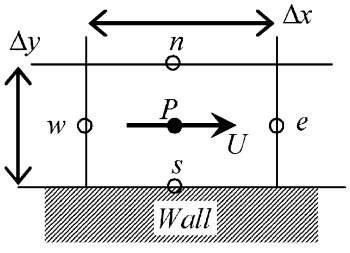

Fig. 1. Near-wall grid arrangement.

where $\overline{S_\phi}$ is the averaged source term over the cell P. Note that x is the wall parallel coordinate while y is the wall normal coordinate. (Although two-dimensional forms are written here, extending them to three-dimensions is straightforward.)

When the wall parallel component of the momentum equation is considered ($\phi = U$) the term $(\Gamma\,\mathrm{d}\phi/\mathrm{d}y)_s$ in Eq. (3) corresponds to the wall shear stress τ_w, while in the energy equation it corresponds to the wall heat flux q_w. Instead of calculating these from the standard discretisation, they are obtained from the algebraic wall-function expressions.

In the case of the transport equation for the turbulence energy k in incompressible flows, the averaged source term over the wall-adjacent cell is written as

$$\overline{S_k} = \overline{\rho P_k - \rho\varepsilon} = \rho(\overline{P_k} - \bar{\varepsilon}). \tag{4}$$

The terms $\overline{P_k}$ and $\bar{\varepsilon}$ thus also need to be provided by the wall-function.

2.1. AWF for smooth wall

Before discussing the extension for rough wall heat transfer, it is useful to summarise the standard AWF by Craft et al. (2002).

In the AWF, the wall shear stress and heat flux are obtained through the analytical solution of simplified near-wall versions of the transport equation for the wall-parallel momentum and temperature. In case of the forced convection regime, the main assumption required for the analytical integration of the transport equations is a prescribed variation of the turbulent viscosity μ_t. (Note that Craft et al., 2002 presented the AWF modelling for buoyant flows introducing a molecular viscosity variation as well.) The distribution of μ_t over the wall-adjacent cell P is modelled as in a one-equation turbulence model:

$$\mu_t = \rho c_\mu k^{1/2}\ell = \rho c_\mu k^{1/2} c_\ell y \simeq \alpha\mu y^*, \tag{5}$$

where ℓ is the turbulent length scale, $\alpha = c_\ell c_\mu$ and $y^* \equiv y k_P^{1/2}/\nu$. In order to consider viscous sub-layer effects, instead of introducing a damping function, the profile of μ_t is modelled as

$$\mu_t = \max\{0, \alpha\mu(y^* - y_v^*)\}, \tag{6}$$

in which μ_t is still linear in y^* and grows from the edge of the viscous sub-layer: $y_v^*(\equiv y_v k_P^{1/2}/\nu)$.

In the context of Fig. 2, the near-wall simplified forms of the momentum and energy equations become

$$\frac{\partial}{\partial y^*}\left[(\mu+\mu_t)\frac{\partial U}{\partial y^*}\right] = \underbrace{\frac{\nu^2}{k_P}\left[\frac{\partial}{\partial x}(\rho UU) + \frac{\partial P}{\partial x}\right]}_{C_U}, \tag{7}$$

$$\frac{\partial}{\partial y^*}\left[\left(\frac{\mu}{Pr} + \frac{\mu_t}{Pr_t}\right)\frac{\partial\Theta}{\partial y^*}\right] = \underbrace{\frac{\nu^2}{k_P}\left[\frac{\partial}{\partial x}(\rho U\Theta) + S_\theta\right]}_{C_T}, \tag{8}$$

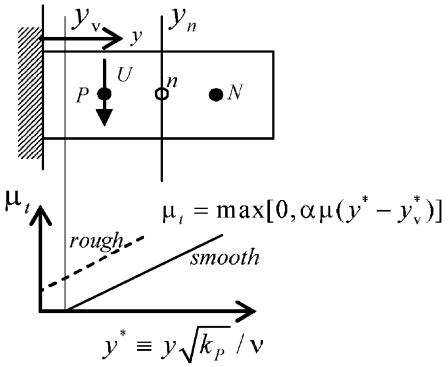

Fig. 2. Near-wall cells.

where Pr_t is a prescribed turbulent Prandtl number, taken as 0.9. The further assumption made is that convective transport and the wall-parallel pressure gradient $\partial P/\partial x$ do not change across the wall-adjacent cell which is a standard treatment in the finite volume method. Thus, the right-hand side (rhs) terms C_U and C_T of Eqs. (7) and (8) can be treated as constant. Then, the equations can be integrated analytically over the wall-adjacent cell giving:

if $y^* < y_v^*$,

$$\frac{dU}{dy^*} = (C_U y^* + A_U)/\mu, \tag{9}$$

$$\frac{d\Theta}{dy^*} = Pr(C_T y^* + A_T)/\mu, \tag{10}$$

$$U = \frac{C_U}{2\mu} y^{*2} + \frac{A_U}{\mu} y^* + B_U, \tag{11}$$

$$\Theta = \frac{PrC_T}{2\mu} y^{*2} + \frac{PrA_T}{\mu} y^* + B_T, \tag{12}$$

if $y^* \geqslant y_v^*$,

$$\frac{dU}{dy^*} = \frac{C_U y^* + A'_U}{\mu\{1 + \alpha(y^* - y_v^*)\}}, \tag{13}$$

$$\frac{d\Theta}{dy^*} = \frac{Pr(C_T y^* + A'_T)}{\mu\{1 + \alpha_\theta(y^* - y_v^*)\}}, \tag{14}$$

$$U = \frac{C_U}{\alpha\mu} y^* + \left\{\frac{A'_U}{\alpha\mu} - \frac{C_U}{\alpha^2\mu}(1 - \alpha y_v^*)\right\} \times \ln[1 + \alpha(y^* - y_v^*)] + B'_U, \tag{15}$$

$$\Theta = \frac{PrC_T}{\alpha_\theta\mu} y^* + \left\{\frac{PrA'_T}{\alpha_\theta\mu} - \frac{PrC_T}{\alpha_\theta^2\mu}(1 - \alpha_\theta y_v^*)\right\} \times \ln[1 + \alpha_\theta(y^* - y_v^*)] + B'_T, \tag{16}$$

where $\alpha_\theta = \alpha\, Pr/Pr_t$. The integration constants A_U, B_U, A_T, B_T etc. are determined by applying boundary conditions at the wall, y_v and the point n. The values at n are determined by interpolation between the calculated node values at P and N, whilst at y_v a monotonic distribution condition is imposed by ensuring that U, Θ and their gradients should be continuous at $y = y_v$. Notice that to determine the integration constants the empirical log-law is not referred to at all and the obtained logarithmic velocity equation (15) includes C_U. The latter implies that the velocity profile has sensitivity to the pressure gradient since C_U includes $\partial P/\partial x$.

The result is that the wall shear stress and wall heat flux can be expressed as

$$\tau_w = \mu\left.\frac{dU}{dy}\right|_w = \mu\frac{k_P^{1/2}}{\nu}\left.\frac{dU}{dy^*}\right|_w = \frac{k_P^{1/2} A_U}{\nu}, \tag{17}$$

$$q_w = -\frac{\rho c_p \nu}{Pr}\left.\frac{d\Theta}{dy}\right|_w = -\frac{\rho c_p \nu}{Pr}\frac{k_P^{1/2}}{\nu}\left.\frac{d\Theta}{dy^*}\right|_w = -\frac{\rho c_p k_P^{1/2} A_T}{\mu}. \tag{18}$$

The local generation rate of k, P_k $(=\nu_t(dU/dy)^2)$, is written as

$$P_k = \begin{cases} 0, & \text{if } y^* < y_v^*, \\ \dfrac{\alpha k_P}{\nu}(y^* - y_v^*)\left(\dfrac{C_U y^* + A'_U}{\mu\{1 + \alpha(y^* - y_v^*)\}}\right)^2, & \text{if } y^* \geqslant y_v^*, \end{cases} \tag{19}$$

which can then be integrated over the wall-adjacent cell to produce an average value $\overline{P_k}$ for use in solving the k equation.

For the dissipation rate ε, the following model is employed:

$$\varepsilon = \begin{cases} 2\nu k_P/y_\varepsilon^2, & \text{if } y < y_\varepsilon, \\ k_P^{1.5}/(c_\ell y), & \text{if } y \geqslant y_\varepsilon. \end{cases} \tag{20}$$

The characteristic dissipation scale y_ε can be defined as $y_\varepsilon^* = 2c_\ell$ to ensure a continuous variation of ε at y_ε. Thus, the cell averaged value is obtained as

$$\bar{\varepsilon} = \begin{cases} 2k_P^2/(\nu y_\varepsilon^{*2}), & \text{if } y_\varepsilon^* > y_n^*, \\ \dfrac{1}{y_n}\left(y_\varepsilon\dfrac{2\nu k_P}{y_\varepsilon^2} + \displaystyle\int_{y_\varepsilon}^{y_n}\frac{k_P^{1.5}}{c_\ell y}\,dy\right) = \frac{k_P^2}{\nu y_n^*}\left[\frac{2}{y_\varepsilon^*} + \frac{1}{c_\ell}\ln\left(\frac{y_n^*}{y_\varepsilon^*}\right)\right], & \text{if } y_\varepsilon^* \leqslant y_n^*. \end{cases} \tag{21}$$

Through numerical experiments, the value of the constant y_v^* was optimised to be 10.7 which corresponds to approximately half the thickness of the conventionally defined viscous sub-layer of $y^+ = 11$. The other model coefficients are listed in Table 1.

2.2. Extension for rough wall turbulent flow and heat transfer

In a rough wall turbulent boundary layer, as shown in Fig. 3, the log-law velocity profile shifts downward depend-

Table 1
Model coefficients

α	c_ℓ	c_μ	y_{vs}^*	y_ε^*	Pr_t^∞
$c_\ell c_\mu$	2.55	0.09	10.7	5.1	0.9

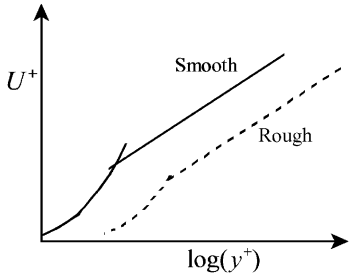

Fig. 3. Surface roughness effects on velocity profile.

ing on the equivalent sand grain roughness height h (Nikuradse, 1933) and written as an empirical formula:

$$U^+ = \frac{1}{\kappa}\ln\frac{y^+}{h^+} + 8.5, \tag{22}$$

for completely rough flows. This implies that the flow becomes more turbulent due to the roughness. It is thus considered that the viscous sub-layer is destroyed in the "fully rough" regime while it partly exists in the "transitional roughness" regime.

In common with conventional wall-functions (e.g., Cebeci and Bradshaw, 1977), the present extension of the AWF strategy to flows over rough surfaces involves the use of the dimensionless roughness height. In this case, however, instead of h^+, h^* is used to modify the near-wall variation of the turbulent viscosity. More specifically, in a rough wall turbulence, y_v^* is no longer fixed at 10.7 and is modelled to become smaller. This provides that the modelled distribution of μ_t shown in Fig. 2 shifts toward the wall depending on h^*. At a certain value of the dimensionless roughness height $h^* = A$, $y_v^* = 0$ is assumed and at $h^* > A$, it is expediently allowed to have a negative value of y_v^* to give a positive value of μ_t at the wall as

$$y_v^* = y_{vs}^*\{1 - (h^*/A)^m\}, \tag{23}$$

where y_{vs}^* is the viscous sub-layer thickness in the smooth wall case. The optimised values for A and m have been determined through a series of numerical experiments and comparisons with available pipe flow data. The resultant form is

$$y_v^* = y_{vs}^*\{1 - (h^*/70)^m\}, \tag{24}$$

with

$$m = \max\left\{\left(0.5 - 0.4\left(\frac{h^*}{70}\right)^{0.7}\right), \left(1 - 0.79\left(\frac{h^*}{70}\right)^{-0.28}\right)\right\}. \tag{25}$$

For $h^* < 70$, the viscosity-dominated sub-layer exists, but with the above modified value for y_v^*. When $h^* > 70$, corresponding to $y_v^* < 0$, it is totally destroyed. Note that although the experimentally known condition for the full rough regime is $h^+ \geqslant 70$, the condition when the viscous sub-layer vanishes from Eq. (24) is $h^* = 70$ that corresponds to $h^+ \simeq 40$ in a typical channel flow case. This is rather consistent with the relation of the viscous sub-layer thicknesses in the smooth wall case. (In the smooth wall case, the viscous sub-layer thickness of $y_v^* = 10.7$ corresponds to approximately half the thickness of the conventionally defined viscous sub-layer of $y^+ = 11$.) It is thus considered that a part of the transitional roughness regime is somehow effectively modelled into the region without the viscous sub-layer by the present strategy due to simply assuming the near-wall turbulence behaviour.

Unlike in a sub-layer over a smooth wall, the total shear stress now includes the drag force from the roughness elements in the inner layer which is proportional to the local velocity squared and becomes dominant away from the wall, compared to the viscous force. In fact, the data reported by Krogstad et al. (1992) and Tachie et al. (2003) showed that the turbulent shear stress away from the wall sometimes became larger than the wall shear stress. This implies that the convective and pressure gradient contributions should be represented somewhat differently across the inner layer, below the roughness element height. Hence, the practice of simply evaluating the rhs of Eq. (7) in terms of nodal values needs modifying. In the present study a simple approach has been taken, by assuming that the total shear stress remains constant across the roughness element height. Consequently, one is led to

$$C_U = \begin{cases} 0, & \text{if } y^* \leqslant h^*, \\ \dfrac{v^2}{k_P}\left[\dfrac{\partial}{\partial x}(\rho UU) + \dfrac{\partial P}{\partial x}\right], & \text{if } y^* > h^*. \end{cases} \tag{26}$$

In the energy equation, Pr_t is also no longer constant over the wall-adjacent cell. The reason for this is that, since the fluid trapped around the roots of the roughness elements forms a thermal barrier, the turbulent transport of the thermal energy is effectively reduced relative to the momentum transport. (The results of the rib-roughened channel flow direct numerical simulation (DNS) by Nagano et al. (2004) support this consideration since their obtained turbulent Prandtl number increases significantly toward the wall in the region between the riblets.) Thus, as illustrated in Fig. 4, although it might be better to model the distribution of Pr_t with a non-linear function, a simple linear profile is assumed in the roughness region of $y \leqslant h$ as

$$Pr_t = Pr_t^\infty + \Delta Pr_t, \tag{27}$$

$$\Delta Pr_t = C_0 \max(0, 1 - y^*/h^*). \tag{28}$$

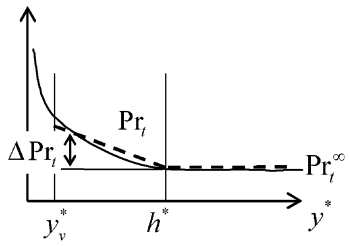

Fig. 4. Modelled turbulent Prandtl number distribution.

After a series of numerical experiments referring to the thermal log-law profiles, the following form for C_0 has been adopted within the roughness elements ($y \leqslant h$):

$$C_0 = \frac{5.5}{1 + (h^*/70)^{6.5}} + 0.6. \tag{29}$$

Over the rest of the field ($y > h$), $Pr_t = Pr_t^{\infty}$ is applied (see Table 1 for the model coefficients). Note that since the turbulent viscosity is defined as zero in the region $y < y_v$, the precise profile adopted for the turbulent Prandtl number in the viscous sub-layer ($y < y_v$) does not affect the computation.

At a high Pr flow ($Pr \gg 1$), the sub-layer, across which turbulent transport of thermal energy is negligible, becomes thinner than the viscous sub-layer. Thus, the assumption that the turbulent heat flux becomes negligible when $y < y_v$, no longer applies. Although this may be corrected through the introduction of an effective molecular Prandtl number (Gerasimov, 2003), the present study does not include this practice for high Pr rough wall heat transfer. Therefore, the present approach is currently valid for heat transfer in flows at $Pr \leqslant 1$.

The analytical solutions of both mean flow and energy equations then can be obtained in the four different cases illustrated in Fig. 5 assuming that the wall-adjacent cell height is always greater than the roughness height. Although one can apply the models of Eqs. (26) and (27) at any node point, limiting them to the wall-adjacent cells is preferable from the numerical view point since it only requires a list of the cells facing to walls for wall boundary conditions. (Despite that, in simple flow cases, the present AWF is still applicable to wall-adjacent cells whose height is lower than the roughness height as discussed in Section 3.1.2.) Even in the case without any viscous sub-layer, case(a), the resultant expressions for τ_w and q_w are of the same form as those of Eqs. (17) and (18). However, different values of A_U and A_T, which are functions of the roughness height, are obtained, corresponding to the four different cases (see Appendix for the detailed derivation process).

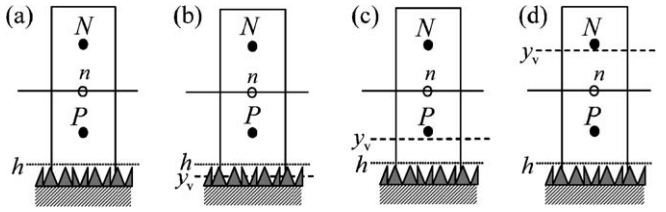

Fig. 5. Near-wall cells over a rough wall: (a) $y_v \leqslant 0$, (b) $0 < y_v \leqslant h$, (c) $h < y_v \leqslant y_n$, (d) $y_n < y_v$.

In Table 2, the cell averaged generation term $\overline{P_k}$ and A_U are listed, introducing $Y^* \equiv 1 + \alpha(y^* - y_v^*)$. Note that Eqs. (20) and (21) are still used for the dissipation, and the integration for $\overline{P_k}$ in Table 2 can be performed as follows:

$$\begin{aligned}\int_a^b (y - y_v)\left(\frac{Cy + A}{1 + \alpha(y - y_v)}\right)^2 \mathrm{d}y &= \left[\frac{C^2}{2\alpha^2}y^2 + \frac{C(2A + Cy_v - 2C/\alpha)}{\alpha^2}y + \frac{(A + Cy_v - C/\alpha)^2}{\alpha^2[1 + \alpha(y - y_v)]}\right.\\ &\left. + \frac{(A + Cy_v - C/\alpha)(A + Cy_v - 3C/\alpha)}{\alpha^2}\ln[1 + \alpha(y - y_v)]\right]_a^b.\end{aligned} \tag{30}$$

Table 2
Cell averaged generation: $\overline{P_k}$, and integration constant: A_U

Case	$\overline{P_k}$
(a) $y_v < 0$	$\frac{\alpha}{\mu^2 y_n^*}\frac{k_P}{\nu}\left\{\int_0^{h^*}(y^* - y_v^*)\left(\frac{A_U}{Y^*}\right)^2 \mathrm{d}y^* + \int_{h^*}^{y_n^*}(y^* - y_v^*)\left(\frac{C_U(y^* - h^*) + A_U}{Y^*}\right)^2 \mathrm{d}y^*\right\}$
(b) $0 \leqslant y_v \leqslant h$	$\frac{\alpha}{\mu^2 y_n^*}\frac{k_P}{\nu}\left\{\int_{y_v^*}^{h^*}(y^* - y_v^*)\left(\frac{A_U}{Y^*}\right)^2 \mathrm{d}y^* + \int_{h^*}^{y_n^*}(y^* - y_v^*)\left(\frac{C_U(y^* - h^*) + A_U}{Y^*}\right)^2 \mathrm{d}y^*\right\}$
(c) $h \leqslant y_v \leqslant y_n$	$\frac{\alpha}{\mu^2 y_n^*}\frac{k_P}{\nu}\int_{y_v^*}^{y_n^*}(y^* - y_v^*)\left(\frac{C_U(y^* - h^*) + A_U}{Y^*}\right)^2 \mathrm{d}y^*$
(d) $y_n \leqslant y_v$	0
	A_U
(a) $y_v < 0$	$\left\{\alpha\mu U_n - C_U(y_n^* - h^*) + C_U\left(\frac{Y_w^*}{\alpha} + h^*\right)\ln[Y_n^*/Y_h^*]\right\}/\ln[Y_n^*/Y_w^*]$
(b) $0 \leqslant y_v \leqslant h$	$\left\{\alpha\mu U_n - C_U(y_n^* - h^*) + C_U\left(\frac{Y_w^*}{\alpha} + h^*\right)\ln[Y_n^*/Y_h^*]\right\}/(\alpha y_v^* + \ln Y_n^*)$
(c) $h \leqslant y_v \leqslant y_n$	$\left\{\alpha\mu U_n - C_U(y_n^* - y_v^*) + C_U\left(\frac{Y_w^*}{\alpha} + h^*\right)\ln Y_n^* - \frac{\alpha}{2}C_U(y_v^{*2} - 2h^* y_v^* + h^{*2})\right\}/(\alpha y_v^* + \ln Y_n^*)$
(d) $y_n \leqslant y_v$	$\left\{\mu U_n - \frac{1}{2}C_U(y_n^{*2} - 2h^* y_n^* + h^{*2})\right\}/y_n^*$

Table 3
Coefficients in Eq. (31)

Case	D_T
(a) $y_v < 0$	$\frac{-\beta_T h^*}{\alpha_T-\beta_T}+\frac{\alpha_T Y_h^{\beta T}}{(\alpha_T-\beta_T)^2}\ln(Y_h^{\alpha T}/\lambda_b)+\frac{1}{\alpha_T}\ln(Y_n^{\alpha T}/Y_h^{\alpha T})$
(b) $0 \leqslant y_v \leqslant h$	$\frac{\alpha_T y_v^*-\beta_T h^*}{\alpha_T-\beta_T}+\frac{\alpha_T Y_h^{\beta T}}{(\alpha_T-\beta_T)^2}\ln(Y_h^{\alpha T}/Y_h^{\beta T})+\frac{1}{\alpha_T}\ln(Y_n^{\alpha T}/Y_h^{\alpha T})$
(c) $h \leqslant y_v \leqslant y_n$	$\frac{1}{\alpha_T}\ln Y_n^{\alpha T}+y_v^*$
(d) $y_n \leqslant y_v$	y_n^*
	E_T
(a) $y_v < 0$	$\frac{h^*-y_n^*}{\alpha_T}+\frac{1}{\alpha_T}\left\{\frac{Y_w^{\alpha T}}{\alpha_T}+h^*-\frac{Y_h^{\alpha T}}{\alpha_T-\beta_T}\left(\frac{\lambda_b\alpha_T}{\alpha_T-\beta_T+1}\right)+\frac{\lambda_b\alpha_T Y_h^{\beta T}}{(\alpha_T-\beta_T)^2}\right\}\ln(Y_n^{\alpha T}/Y_h^{\alpha T})$ $+\frac{\alpha_T\lambda_b Y_h^{\beta T}}{(\alpha_T-\beta_T)^3}\ln(Y_h^{\alpha T}/\lambda_b)-\frac{h^*}{\alpha_T-\beta_T}\left(1+\frac{\beta_T h^*}{2}+\frac{\beta_T\lambda_b}{\alpha_T-\beta_T}\right)$
(b) $0 \leqslant y_v \leqslant h$	$\frac{h^*-y_n^*}{\alpha_T}+\frac{1}{\alpha_T}\left\{\frac{Y_w^{\alpha T}}{\alpha_T}+h^*-\frac{Y_h^{\alpha T}}{\alpha_T-\beta_T}\left(\frac{\lambda_b\beta_T}{\alpha_T-\beta_T}+1\right)+\frac{\lambda_b\alpha_T Y_h^{\beta T}}{(\alpha_T-\beta_T)^2}\right\}\ln(Y_n^{\alpha T}/Y_h^{\alpha T})$ $+\frac{\alpha_T\lambda_b Y_h^{\beta T}}{(\alpha_T-\beta_T)^3}\ln(Y_h^{\alpha T}/Y_h^{\beta T})-\frac{h^*}{\alpha_T-\beta_T}\left(1+\frac{\beta_T h^*}{2}+\frac{\beta_T\lambda_b}{\alpha_T-\beta_T}\right)+\frac{y_v^*}{\alpha_T-\beta_T}\left(\frac{\alpha_T Y_h^{\beta T}}{\alpha_T-\beta_T}-\frac{\alpha_T y_v^*}{2}\right)$
(c) $h \leqslant y_v \leqslant y_n$	$\frac{y_v^*-y_n^*}{\alpha_T}-y_v^{*2}/2+\frac{Y_w^{\alpha T}}{\alpha_T^2}\ln Y_n^{\alpha T}$
(d) $y_n \leqslant y_v$	$-y_n^{*2}/2$

For heat transfer, the resultant form of the integration constant A_T can be written as

$$A_T = \{\mu(\Theta_n - \Theta_w)/Pr + C_T E_T\}/D_T \tag{31}$$

where the coefficients D_T and E_T are listed in Table 3, defining $\alpha_T \equiv \alpha Pr/(Pr_t^\infty)$, $\beta_T \equiv C_0/(h^* Pr_t^\infty)$, $Y^{\alpha T} \equiv 1 + \alpha_T(y^* - y_v^*)$, $Y^{\beta T} \equiv 1 + \beta_T(y^* - y_v^*)$, and $\lambda_b \equiv Y_0^{\alpha T} + \beta_T h^*$.

In the case of a constant wall heat flux condition, the wall temperature is obtained by rewriting Eqs. (18) and (31) as

$$\Theta_w = \Theta_n + \frac{Prq_w}{\rho c_p k_P^{1/2}} D_T + \frac{PrC_T E_T}{\mu}. \tag{32}$$

3. Results and discussion

The computational fluid dynamics (CFD) codes used in this study are in-house finite-volume codes: TEAM (Huang and Leschziner, 1983) and STREAM (Lien and Leschziner, 1994a). The former is used to compute turbulent pipe and flat plate boundary layer flows and the latter is used to compute turbulent channel, flat and curved boundary layer and separating flows. Both codes employ the SIMPLE pressure-correction algorithm (Patankar, 1980). TEAM uses an orthogonal staggered grid arrangement whilst STREAM uses a non-orthogonal collocated one employing Rhie and Chow's (1983) interpolation and the third order MUSCL type scheme for convection terms (Lien and Leschziner, 1994b). The AWF has been implemented with the "standard" linear k–ε (Launder and Spalding, 1974; Launder and Sharma, 1974: LS) and also with a cubic non-linear k–ε model (Craft et al., 1996: CLS). (Although the LS and the CLS models are LRN models, with the wall-function grids, the LRN parts of the model terms do not contribute to the computation results.) For comparison, flow predictions have also been occasionally obtained using the LRN models. For the turbulent heat flux in the core-region, the usual eddy diffusivity model with a prescribed turbulent Prandtl number $Pr_t = 0.9$ is used.

3.1. Wall parallel flows

3.1.1. Pipe flows

Fig. 6 compares the presently predicted friction coefficient and the experimental correlation for turbulent pipe flows, known as the Moody chart (Moody, 1944). The turbulence is modelled by the linear k–ε model with the AWF. In the range of $h/D = 0$–0.05 (D: pipe diameter) and $Re = 8000$–10^8, it is confirmed that the AWF performs reasonably well over a wide range of Reynolds numbers and roughness heights. (The number of computational grid nodes ranged from 12 to 200 across the pipe radius for Reynolds numbers ranging from 8000 to 10^8, whilst the

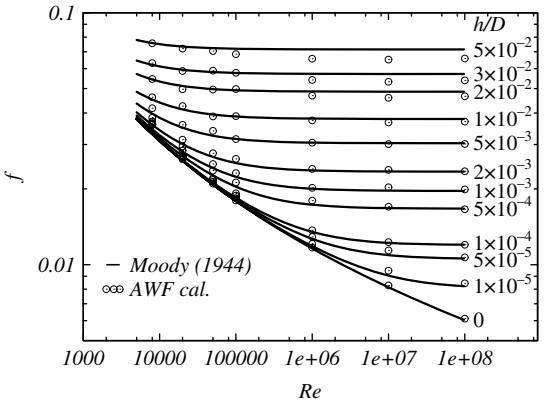

Fig. 6. Friction factors in pipe flows (Moody chart).

value of y^* at the wall-adjacent node ranged from 50 to 500.)

3.1.2. Channel flows

Fig. 7(a) shows the mean velocity distribution in turbulent channel flows at $Re = 10^5$. In the case of a smooth wall, $h/D = 0$ (D: channel height), the HRN k–ε model with the AWF reproduces the result of the LRN LS k–ε model regardless of the near-wall cell size. The meshes used for the smooth wall case have 49, 19 and 14 nodes across the channel, resulting in near-wall cell heights of $\Delta y_1/D = 0.015$, 0.045 and 0.09 which respectively correspond to $y^+ = 66$, 202 and 408. In the rough wall cases with $h/D = 0.01$ and 0.03, it is clear that the AWF reproduces the log-law distribution for fully rough wall flows by Eq. (22) and Cebeci and Bradshaw's (1977):

$$U^+ = \frac{1}{\kappa}\ln y^+ + 5.2 - \left(5.2 - 8.5 + \frac{1}{\kappa}\ln h^+\right) \times \sin(0.4258[\ln h^+ - 0.811]) \quad (33)$$

for $2.25 < h^+ < 90$. Note that in the case of $h/D = 0.01$, the corresponding roughness Reynolds number is $h^+ = 63$ which is still in the transitional roughness regime, while $h/D = 0.03$ corresponds to $h^+ = 218$ which is well in the fully rough regime. For each roughness case, profiles from more than one grid are plotted. (In fact, for $h/D = 0.01$ the results by three grids of $\Delta y_1/D = 0.015$, 0.045 and 0.09, which respectively correspond to $y^+ = 94$, 286 and 576, are plotted while for $h/D = 0.03$ the results by two grids of $\Delta y_1/D = 0.045$ and 0.09, which respectively correspond to $y^+ = 334$ and 671, are plotted.) Since the AWF is quite insensitive to near-wall grid size, discrepancies between the profiles are hardly seen.

Fig. 7(b) shows the corresponding mean temperature distribution to Fig. 7(a) at $Pr = 0.71$. In the smooth wall case, with any grid spacing, the AWF well reproduces the result of the LRN LS k–ε model and the log-law profile of Johnk and Hanratty (1962):

$$\Theta^+ = 3.3 + 2.21\ln y^+. \quad (34)$$

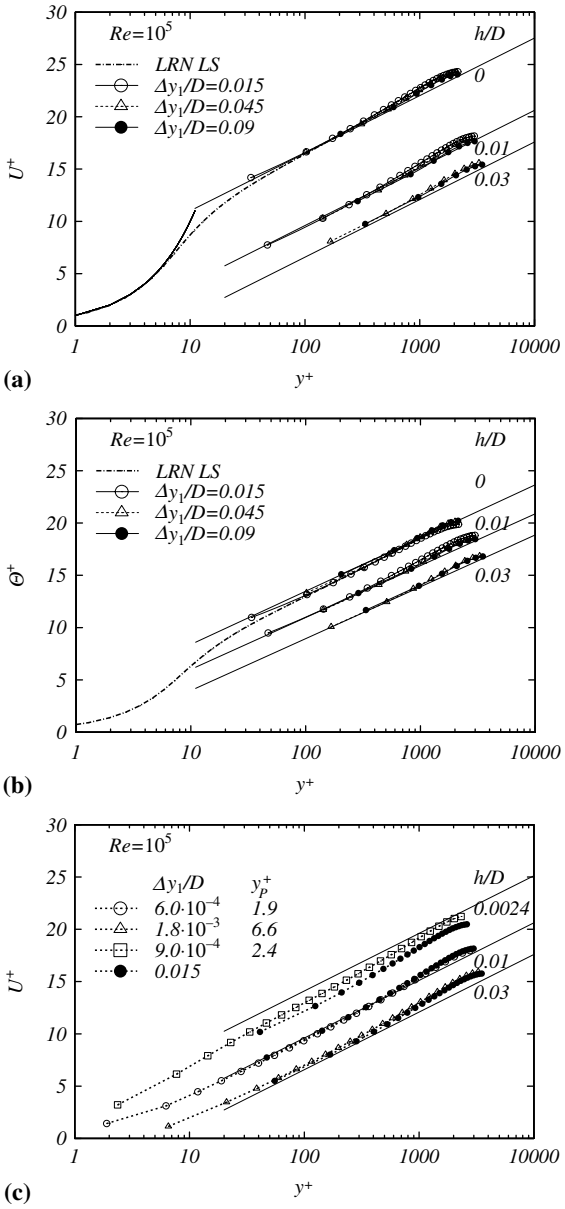

Fig. 7. Mean velocity and temperature distribution in channel flows at $Pr = 0.71$; lines with symbols: AWF + k–ε, solid thin lines: log-law profiles.

In the cases of rough walls, it is also clear that with any near-wall grid size, the AWF well reproduces the log-law distribution for rough walls (Kays and Crawford, 1993):

$$\Theta^+ = \frac{1}{0.8h^{+-0.2}Pr^{-0.44}} + \frac{Pr_t}{\kappa}\ln\frac{32.6y^+}{h^+}, \quad (35)$$

where $Pr_t = 0.9$.

Although it is recommended to employ a computational mesh whose wall-adjacent cells are always higher than the roughness elements, not such a mesh is still applicable for flow field computations with the AWF. In fully rough wall flows, the requirement at the wall-adjacent cell is $U_P^+ > 0$, then from Eq. (22) one can obtain:

$$\ln\frac{y_P^+}{h^+} > -8.5\kappa, \quad y_P^+ > h^+\exp(-8.5\kappa) \simeq 0.03h^+. \tag{36}$$

In the cases of $h/D = 0.01, 0.03$, corresponding to $h^+ = 63, 218$, Eq. (36) suggests $y_P^+ > 1.89, 6.54$, respectively. (Although the case of $h^+ = 63$ is in the transitional roughness regime, its log-law profile is nearly the same as that by Eq. (22).) Fig. 7(c) confirms these conditions. In fact, by the meshes, whose first nodes locate at 1.9 and 6.6 in wall unit, the AWF produces almost identical profiles to those by a much coarser mesh.

In the transitional roughness regime of $h/D = 0.0024(h^+ = 13)$, corresponding to case (b) of Fig. 5, the viscous sub-layer exists and it is readily understandable that the wall-adjacent cell height should be greater than the sub-layer thickness otherwise no roughness effects are considered in turbulence generation. In this case, since the viscous sub-layer thickness by Eq. (24) is $y_v^* = 4.7$ which corresponds to $y_v^+ = 4.1$, the wall-adjacent cell height should be greater than this value. The profile by the mesh of $y_P^+ = 2.4$ (whose wall-adjacent cell height is twice of this value) generally accords with that by the coarser mesh, though the agreement is not so good as that of the other cases.

In the case of $h < y_v$, corresponding to cases (c) and (d) in Fig. 5, when the wall-adjacent cell height is lower than the roughness height, the solution tends to be a smooth wall one. Therefore, if one requires the lowest limit of the wall-adjacent cell height y_n^+ for the AWF:

$$y_n^+ > \max(0.06h^+, \min(h^+, y_v^+)) \tag{37}$$

is advised for wall attached flows. (Note that a cell-centered mesh system is assumed.) However, since the grid sensitivity in thermal field results (not shown) is not similar to that of the flow field, making wall-adjacent cells higher than the roughness is strongly recommended to obtain reasonable thermal-field results.

3.1.3. Flat plate boundary layer flows

Hosni et al. (1991) measured Stanton number St distribution in zero pressure gradient isothermally heated rough wall boundary layer flows. They arranged hemispherical roughness elements on the base of their wind tunnel. According to Schlichting (1979), their cases of $L/d = 2$, 4, respectively correspond to 0.63, 0.1 mm of the equivalent sand grain roughness heights h. Consequently, the flow regimes correspond to the fully rough ($h^+ \simeq 120$) and the transitional roughness regimes ($h^+ \simeq 16$), respectively. For these developing boundary layer flows, the computational mesh of 200×40 is used to cover the region of $0 < Re_x < 10^7$. All the wall-adjacent cells are set to be higher than the equivalent sand grain roughness heights. (Although it is not shown here, the sensitivity to wall-adjacent cell heights shows a similar tendency to that in channel flows.)

Fig. 8 compares the friction coefficient C_f distribution obtained by the AWF with the standard k–ε model and the experimental results. It is confirmed that the predicted profiles are reasonable for the rough wall cases as well as the smooth wall case. (Although it is not shown here, more comprehensive comparisons between the predictions and the experimental correlations of boundary layers further confirm the reliability of the present scheme.)

Fig. 9 shows the comparison in the distribution of St. It can be seen that the present predictions accord well with the experimentally obtained values. For the surface with $L/d = 4$, the increase in St over the smooth wall case is about 40%; and for $L/d = 2$ the increase is about 75%. This increase of St due to the roughness is correctly predicted. Note that the profile of the experimental smooth wall case is from the correlation shown in Hosni et al. (1991):

$$St = 0.185(\log_{10} Re_x)^{-2.584} Pr^{-0.4}. \tag{38}$$

Fig. 10 compares the mean temperature distribution at the point of $Re_x = 10^6$. The log-law lines are from Eq. (35). Although the predicted profiles are a little lower than the log-law profiles, the agreement is satisfactory.

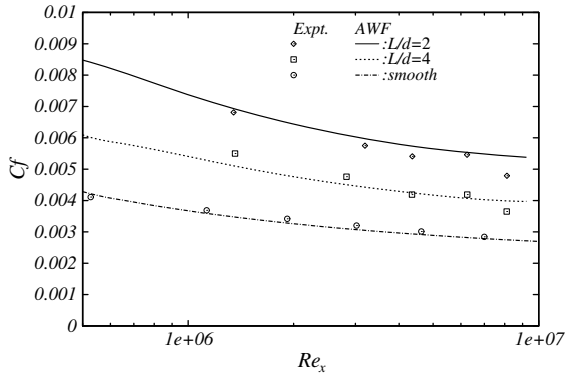

Fig. 8. Friction coefficient C_f in rough wall boundary layers.

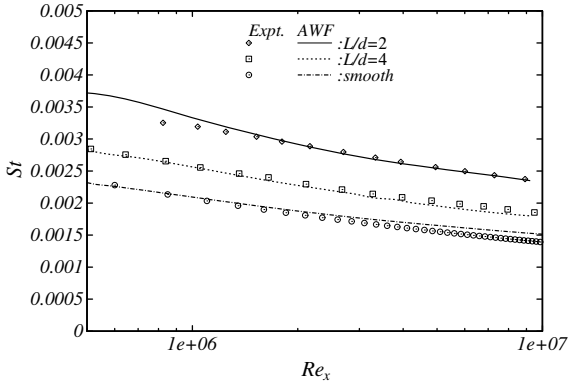

Fig. 9. Stanton number distribution in rough wall boundary layers at $Pr = 0.71$.

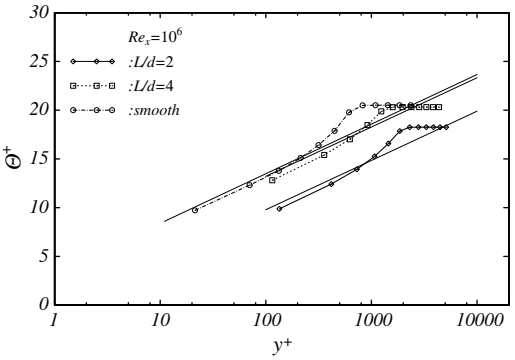

Fig. 10. Mean temperature in rough wall boundary layers at $Pr = 0.71$; lines with symbols: AWF + k–ε, solid thin lines: log-law profiles.

3.1.4. Curved wall boundary layer flows

Heat transfer along curved surfaces is very common and important in engineering applications such as in heat sinks and around turbine blades. Thus, although the AWF itself does not explicitly include sensitivity to streamline curvature, it is useful to confirm its performance when applied in combination with a turbulence model which does capture streamline curvature effects. Hence, the turbulence model used here is the cubic non-linear k–ε model (CLS).

For comparison, the rough wall heat transfer experiments over a convex surface by Turner et al. (2000) are chosen. The flow geometry is shown in Fig. 11. (Since its curved section is so short, it is impossible to discuss fully developed characteristics of the curved flow. However, as far as the present authors are aware, other such fundamental measurements have not been reported in the literature.) The working fluid was air at room temperature and the wall was isothermally heated. The comparison is made in the cases of trapezoidal shaped roughness elements. According to Turner et al., the equivalent sand grain roughness height h is 1.1 times the element height. The computational mesh used is 90×20 whose wall-adjacent cell height is 5 mm which is greater than the equivalent sand grain roughness heights. (A fine mesh of 90×50 whose wall-adjacent cell height is 1 mm is also used to confirm the sensitivity to the wall-adjacent cell heights. The corresponding discussion is addressed in the following paragraph.)

Fig. 12 compares the heat transfer coefficient α distribution under zero pressure gradient conditions. Fig. 12(a) shows the case of $h = 0.55$ mm. The inlet velocities of

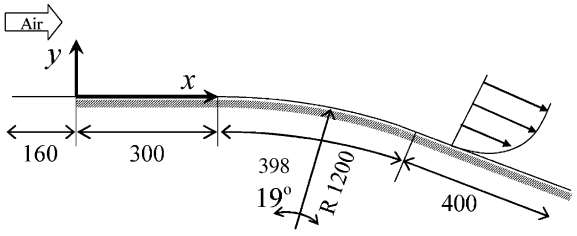

Fig. 11. Flow geometry of the convex rough wall boundary layers of Turner et al. (2000).

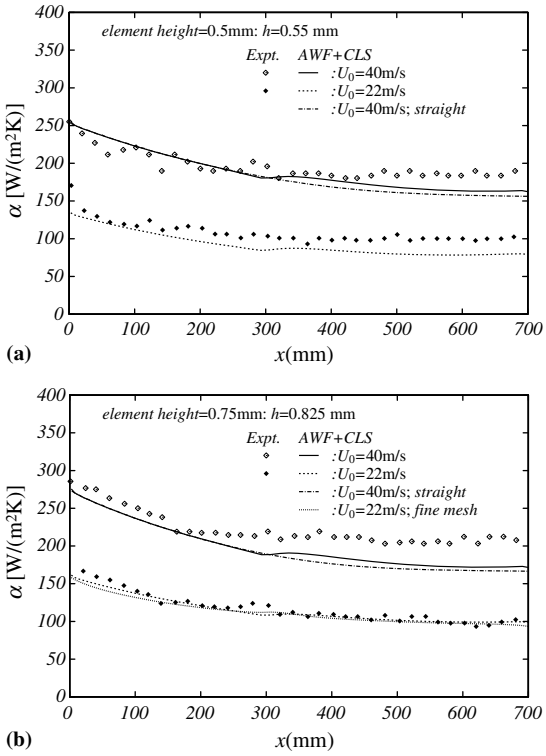

Fig. 12. Heat transfer coefficient distribution in convex rough wall boundary layers at $Pr = 0.71$.

$U_0 = 40$, 22 m/s respectively correspond to $h^+ \simeq 90$, 50 and thus they are in the full and the transitional roughness regimes. In the case of $h = 0.825$ mm, shown in Fig. 12(b), $U_0 = 40$, 22 m/s correspond to $h^+ \simeq 135$, 80 which are both in the fully rough regime. From the comparisons, although there can be seen some discrepancy, it is recognised that the agreement between the experiments and the predictions is acceptable in both the full and transitional roughness regimes. In Fig. 12(b), the result by the fine mesh of 90×50 whose wall-adjacent cell height is 1 mm is also plotted for the case of $U_0 = 22$ m/s. It is readily seen that the AWF is rather insensitive to the near-wall mesh resolution in such a flow case since two profiles from very different resolutions are nearly the same.

Fig. 12 also shows the effects of the wall curvature on the heat transfer coefficients in the case of $U_0 = 40$ m/s. (The curved section is in the region of 300 mm $\leqslant x \leqslant$ 698 mm.) Although the curvature effects observed are not large, since the curvature is not very strong, they are certainly predicted by the present computations with the AWF and cubic non-linear k–ε model. Turner et al. (2000) reported that the curvature appeared to cause an increase of 2–3% in the heat transfer coefficient α. Computations are consistent with this experimental observation. Note that the present curvature effects are of the entrance region of the convex wall. Due to the sudden change of the curvature rate, the pressure gradient becomes locally stronger near the starting point of the convex wall resulting in flow acceleration and thus heat transfer enhancement.

3.2. Separating flows

Since to the knowledge of the authors, no useful heat transfer data of separating flows over rough walls have been published in the literature, the present model validation has been performed for flow fields only.

3.2.1. Sand dune flow

Fig. 13 shows the geometry and a computational mesh used for a water flow over a sand dune of van Mierlo and de Ruiter (1988). Their experimental rig consisted of a row of 33 identical two-dimensional sand dunes covered with sand paper, whose averaged sand grain height was 2.5 mm. Since they measured the flow field around one of the central dunes of the row, streamwise periodic boundary conditions are imposed in the computation. In the experiments, the free surface was located at $y = 292$ mm and the bulk mean velocity was $U_b = 0.633$ m/s. Thus, the Reynolds number based on U_b and the surface height was 175,000. In this flow, a large recirculation zone appears behind the dune. Due to the flow geometry, the separation point is fixed at $x = 0$ m as in a back-step flow.

Fig. 14 compares the predicted friction velocity distribution on meshes of 330×50, 165×50 and 165×25. In the finest and coarsest meshes, the heights of the first cell facing the wall are respectively 4 mm and 8 mm which are larger than the grain height of 2.5 mm which corresponds to $h^+ \simeq 75$ at the inlet. The turbulence model applied is the cubic CLS k–ε model with the differential length-scale correction term for the dissipation rate equation (Iacovides and Raisee, 1999). The lines of the predicted profiles are almost identical to one another, proving that the AWF is rather insensitive to the computational mesh. (In the following discussions on flow field quantities, results by the finest mesh of 330×50 are used.)

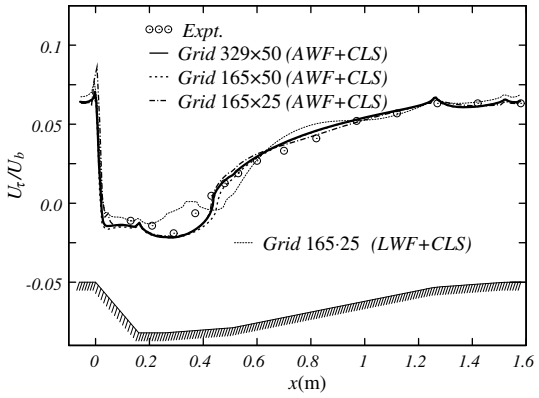

Fig. 14. Friction velocity over the sand dune.

Fig. 14 also shows the result by the log-law wall-function (LWF). Although the log-law wall-function, Eq. (22) should perform reasonably in flat plate boundary layer type of flows, it is obvious that the LWF produces an unstable wiggled profile in the recirculating region of $0\text{ m} < x < 0.6\text{ m}$. The computational costs by the AWF and the LWF are almost the same as each other, with the more complex algebraic expressions of the AWF requiring slightly more processing time.

Fig. 15 compares flow field quantities predicted by the CLS and the LS models with the AWF. In the distribution of the mean velocity and the Reynolds shear stress, both models agree reasonably well with the experiments as shown in Figs. 15(a) and (b) while the CLS model predicts the streamwise normal stress better than the LS model (Fig. 15(c)). These predictive trends of the models are consistent with those in separating flows by the original LRN versions reported by Craft et al. (1999) and thus it is confirmed that coupling with the AWF preserves the original capabilities of the LRN models.

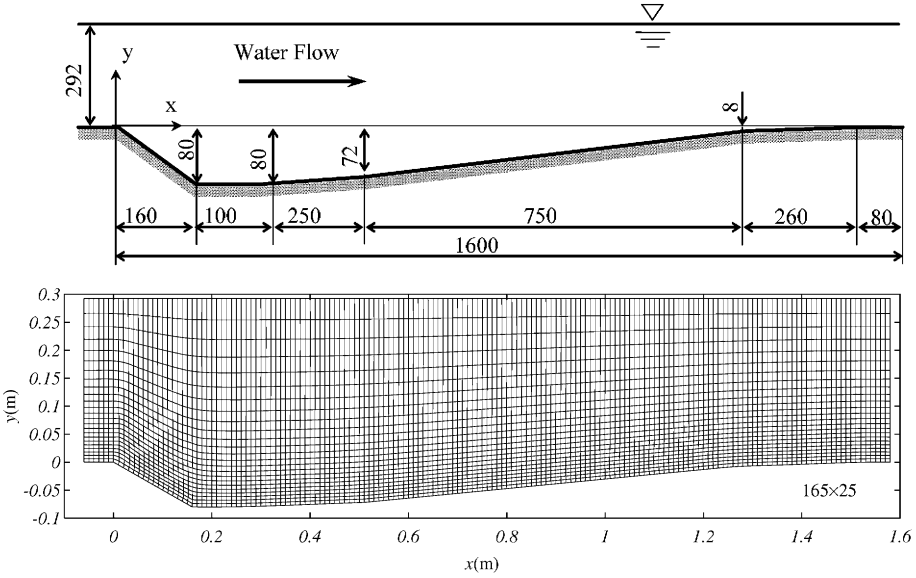

Fig. 13. Dune profile and computational grid.

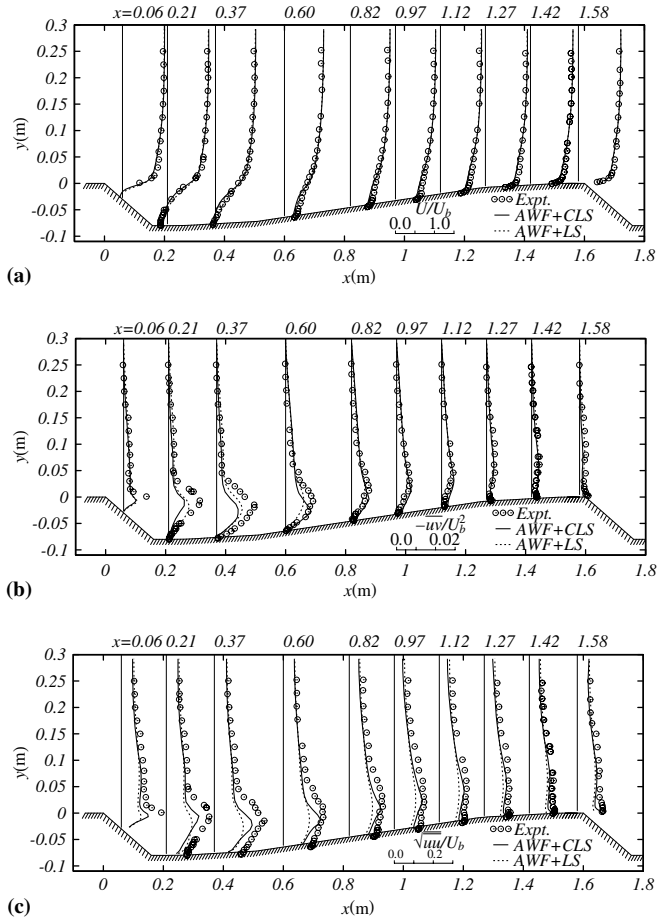

Fig. 15. Mean velocity and Reynolds stress distribution of the sand dune flow.

3.2.2. Ramp flow

Fig. 16 illustrates the flow geometry and a typical computational mesh (220×40) used for the computations of the channel flows with a ramp on the bottom wall by Song et al. (2000) and Song and Eaton (2002). A two-dimensional wind tunnel whose height was 152 mm with a ramp (height $H = 21$ mm, length $L = 70$ mm, radius 127 mm) was used in their experiments. Air flowed from the left at a free stream velocity $U_e = 20$ m/s with developed turbulence ($Re_\theta = 3400$ at $x = 0$ mm for the smooth wall case; $Re_\theta = 3900$ for the rough wall case). Since for the rough wall case sand paper with an averaged grain height of 1.2 mm, which corresponds to $h^+ \simeq 100$ at $x = 0$ mm, covered the ramp part, the height of the first computational cell from the wall is set as 1.5 mm. (Note that since the location of the separation point is not fixed in this flow case, the grid sensitivity test, which is not shown here, suggests that unlike in the other flow cases large wall-adjacent cell heights affect prediction of the recirculation zone.) This flow field includes an adverse pressure gradient along the wall and a recirculating flow whose separation point is not fixed, unlike in the sand dune flow. The measured velocity fields implied that the recirculation region extended between $0.74 \leqslant x'(:x/L) \leqslant 1.36$ and $0.74 < x' \leqslant 1.76$ in the smooth and rough wall cases respectively. Thus relatively finer streamwise resolution is applied to the computational mesh around the ramp part.

Fig. 17 compares the predicted pressure coefficients of the smooth wall case by the AWF and the standard log-law wall-function (LWF) with the results of the LRN computation. The turbulence model used is the CLS model. The first grid nodes from the wall (y_1) are located at

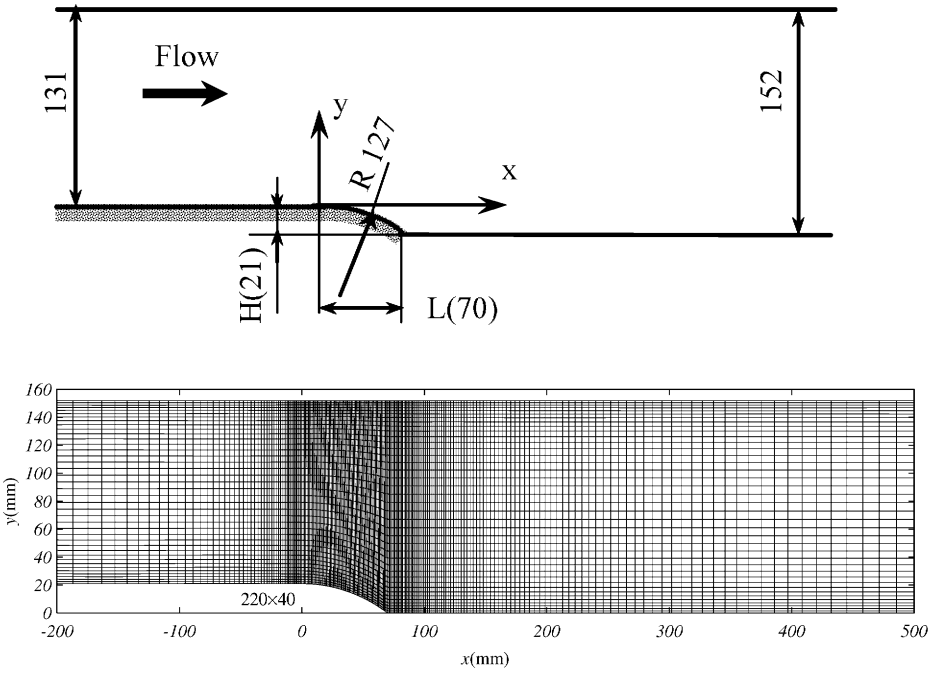

Fig. 16. Ramp geometry and computational grid.

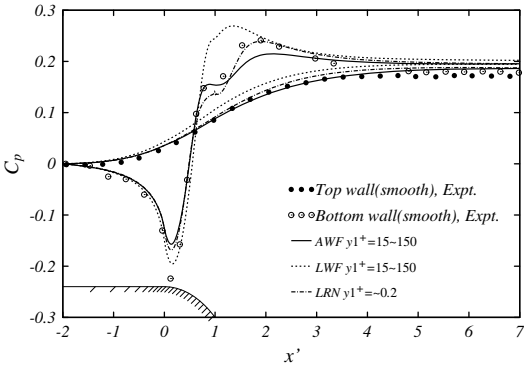

Fig. 17. Pressure coefficient distribution of the smooth ramp flow; CLS is used in all the computations.

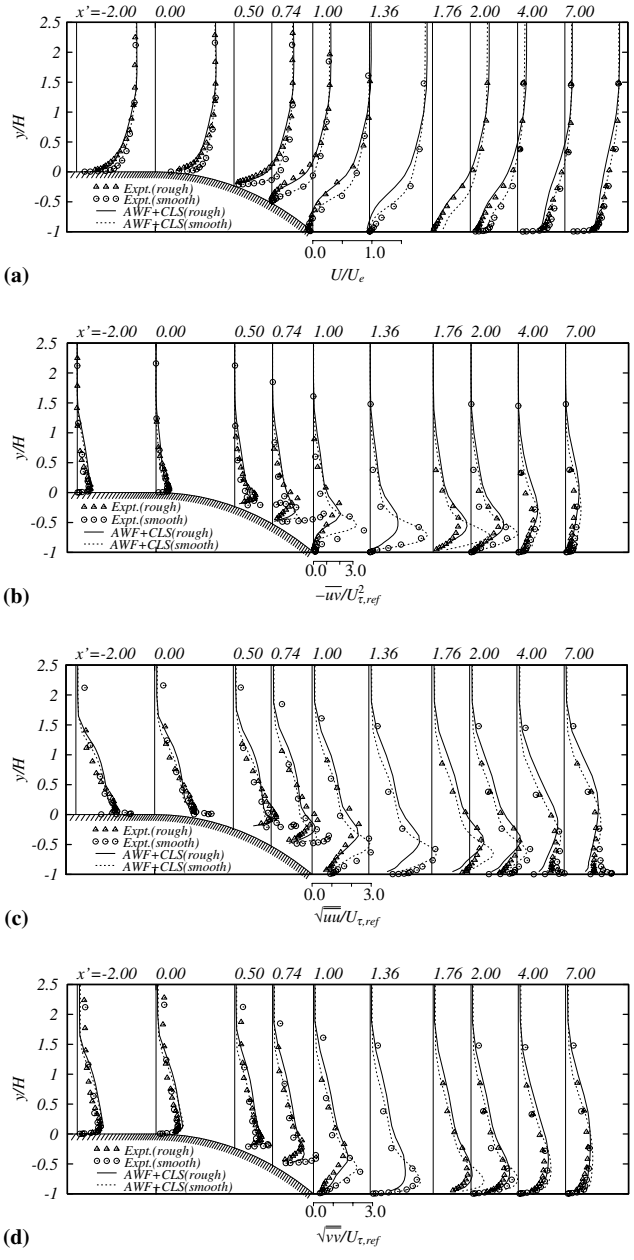

Fig. 18. Mean velocity and Reynolds stress distribution of the ramp flow.

$y_1^+ = 15$–150 for the wall function models while those for the LRN are located at $y_1^+ \leqslant 0.2$. (The mesh used for the LRN case has 100 cells in the y direction.) Obviously, the AWF produces profiles that are closer to those of the experiment than the profiles of the LWF model. The AWF reasonably captures the effects of adverse pressure gradients due to the inclusion of the sensitivity to pressure gradients in its form. Hence, its predictive tendency is similar to that of the LRN model.

Fig. 18(a) compares the mean velocity profiles for both the smooth and rough wall cases. For both the cases, the agreement between the experiments and the predictions by the AWF coupled to the CLS model is reasonably good. The predicted recirculation zones are $0.69 < x' < 1.40$ and $0.57 < x' < 1.60$, in the smooth and rough wall cases, respectively. They, however, do not correspond well with the experimentally estimated ones. Figs. 18(b)–(d) compare the distribution of the Reynolds stresses at the corresponding locations to those in Fig. 18(a). (The values are normalised by the reference friction velocity $U_{\tau,\mathrm{ref}}$ at $x' = -2.0$.) The agreement between the prediction and the experiments is again reasonably good for each quantity.

4. Concluding remarks

The analytical wall-function, which had been developed for application to problems with smooth walls, has been extended to account for the effects of fine-grain surface roughness on turbulence and heat transfer. The overall strategy of the wall-function derivation and application has been retained. The extended scheme has been validated in fully developed pipe, channel and developing boundary layer flows over a wide range of Reynolds numbers and roughness element heights as well as separating flows over a sand dune and a round ramp. The concluding remarks from the present study are

(1) The effects of wall roughness on turbulence and heat transfer are considered by employing functional forms of equivalent sand grain roughness for the non-dimensional thickness of the modelled viscous sub-layer and the turbulent Prandtl number immediately adjacent to the wall.
(2) The present AWF model can be applied successfully to turbulent attached and separated flows over rough surfaces. Although it does not include the conventional log-laws, the AWF accurately reproduces the rough wall log-law profiles of mean velocities and temperatures without grid dependency.
(3) The proposed AWF performs well with both linear and non-linear k–ε models while the predictive accuracy depends on the turbulence model employed in the main flow field. Although it is at least necessary to resolve the flow structure such as a near-wall separation bubble, the sensitivity to near wall grid resolution is low. This is particularly true for wall attached flows.

(4) The computational cost required for the AWF is comparable to that of the standard log-law wall-function.

Acknowledgements

The authors are grateful to Prof. B.E. Launder at The University of Manchester for his suggestions when they planned this research programme. The original computer codes used in this study were kindly provided by Drs. A. Gerasimov and C.M.E. Robinson at The University of Manchester. The information on the DNS data of rib-roughened turbulent channel flows from Dr. H. Hattori at Nagoya Institute of Technology was very helpful.

Appendix

The analytical integration of the momentum and energy equations: Eqs. (7) and (8), is performed in the four different cases illustrated in Fig. 5. The process for the case (a) $y_v < 0$ is as follows.

The integration of Eq. (7) with Eq. (26) is

if $y^* \leqslant h^*$

$$\frac{dU}{dy^*} = \frac{A_U}{\mu\{1+\alpha(y^*-y_v^*)\}} = \frac{A_U}{\mu Y^*}, \tag{39}$$

$$U = \frac{A_U}{\alpha\mu}\ln Y^* + B_U. \tag{40}$$

At a wall: $y^* = 0$, the condition $U = 0$ leads to

$$B_U = -\frac{A_U}{\alpha\mu}\ln(1-\alpha y_v^*) = -\frac{A_U}{\alpha\mu}\ln Y_w^*. \tag{41}$$

When $h^* < y^*$, the integration leads to

$$\frac{dU}{dy^*} = \frac{C_U y^* + A'_U}{\mu Y^*}, \tag{42}$$

$$U = \frac{C_U}{\alpha\mu}y^* + \left(\frac{A'_U}{\alpha\mu} - \frac{Y_w^* C_U}{\alpha^2\mu}\right)\ln Y^* + B'_U. \tag{43}$$

Then, a monotonic distribution condition of dU/dy^* and U at $y^* = h^*$ gives

$$\frac{A_U}{\mu Y_h^*} = \frac{C_U h^* + A'_U}{\mu Y_h^*}, \tag{44}$$

$$\frac{A_U}{\alpha\mu}\ln Y_h^* + B_U = \frac{C_U}{\alpha\mu}h^* + \left(\frac{A'_U}{\alpha\mu} - \frac{Y_w^* C_U}{\alpha^2\mu}\right)\ln Y_h^* + B'_U. \tag{45}$$

Since at $y^* = y_n^*$ the velocity is $U = U_n$ (U_n is obtainable by interpolating the calculated node values at P, N),

$$U_n = \frac{C_U}{\alpha\mu}y_n^* + \left(\frac{A'_U}{\alpha\mu} - \frac{Y_w^* C_U}{\alpha^2\mu}\right)\ln Y_n^* + B'_U. \tag{46}$$

The integration constants A_U, B_U, A'_U, B'_U are thus easily obtainable by solving Eqs. (41) and (44)–(46).

In this case, the wall shear stress τ_w is written as

$$\tau_w = (\mu+\mu_t)\left.\frac{dU}{dy}\right|_{y=0} = \mu Y_w^* \frac{k_P^{1/2}}{\nu}\left.\frac{dU}{dy^*}\right|_{y^*=0} = \frac{k_P^{1/2}A_U}{\nu}, \tag{47}$$

whose resultant form is the same as Eq. (17) and can be calculated with A_U.

Since the cell averaged production term $\overline{P_k}$ of the turbulence energy k is written as

$$\begin{aligned}\overline{P_k} &= \frac{1}{y_n}\left\{\int_0^h \nu_t\left(\frac{dU}{dy}\right)^2 dy + \int_h^{y_n}\nu_t\left(\frac{dU}{dy}\right)^2 dy\right\}\\ &= \frac{\alpha}{y_n^*}\frac{k_P}{\nu}\left\{\int_0^{h^*}(y^*-y_v^*)\left(\frac{dU}{dy^*}\right)^2 dy^*\right.\\ &\quad\left.+\int_{h^*}^{y_n^*}(y^*-y_v^*)\left(\frac{dU}{dy^*}\right)^2 dy^*\right\},\end{aligned} \tag{48}$$

it can be calculated by substituting dU/dy^* with Eqs. (39) and (42).

As for the thermal field, when $y^* \leqslant h^*$, applying Eqs. (27) and (28) to the energy equation: Eq. (8), one can lead to

$$\frac{\partial}{\partial y^*}\left[\left\{\frac{\mu}{Pr} + \frac{\alpha\mu(y^*-y_v^*)}{Pr_t^\infty + C_0(1-y^*/h^*)}\right\}\frac{\partial\Theta}{\partial y^*}\right] = C_T. \tag{49}$$

Its integration follows:

$$\left\{\frac{\mu}{Pr} + \frac{\alpha\mu(y^*-y_v^*)}{Pr_t^\infty + C_0(1-y^*/h^*)}\right\}\frac{d\Theta}{dy^*} = C_T y^* + A_T, \tag{50}$$

$$\frac{d\Theta}{dy^*} = \frac{\{1+\beta_T(h^*-y^*)\}(C_T y^* + A_T)}{1+\alpha_T(y^*-y_v^*)+\beta_T(h^*-y^*)}\frac{Pr}{\mu}. \tag{51}$$

The further integration leads to

$$\begin{aligned}\Theta = &-\left\{\frac{C_T\lambda_b\beta_T}{(\alpha_T-\beta_T)^2} - \frac{C_T(1+\beta_T h^*)+\beta_T A_T}{\alpha_T-\beta_T}\right\}\frac{Pr}{\mu}y^* + \frac{PrC_T\beta_T}{2\mu(\alpha_T-\beta_T)}y^{*2}\\ &+\left[\frac{C_T\lambda_b^2\beta_T}{(\alpha_T-\beta_T)^3} - \frac{\lambda_b\{C_T(1+\beta_T h^*)+\beta_T A_T\}}{(\alpha_T-\beta_T)^2}\right.\\ &\left.+\frac{(1+\beta_T h^*)A_T}{\alpha_T-\beta_T}\right]\frac{Pr}{\mu}\ln[(\alpha_T-\beta_T)y^*+\lambda_b] + B_T.\end{aligned} \tag{52}$$

When $y^* > h^*$,

$$\frac{d\Theta}{dy^*} = \frac{Pr(C_T y^* + A'_T)}{\mu\{1+\alpha_T(y^*-y_v^*)\}} = \frac{Pr(C_T y^* + A'_T)}{\mu Y^{\alpha T}}, \tag{53}$$

$$\Theta = \frac{PrC_T}{\mu\alpha_T}y^* + \frac{Pr}{\mu}\left\{\frac{A'_T}{\alpha_T} - \frac{C_T Y_w^{\alpha T}}{\alpha_T^2}\right\}\ln Y^{\alpha T} + B'_T. \tag{54}$$

The integration constants A_T, B_T, A'_T, B'_T are readily obtainable by Eqs. (51)–(54) imposing the boundary conditions ($\Theta|_{y=0} = \Theta_w, \Theta|_{y=y_n} = \Theta_n$) and a monotonic distribution condition of $d\Theta/dy^*$ and Θ at $y^* = h^*$ as in the flow field.

In the case of a constant wall temperature, the wall heat flux q_w can be calculated as

$$q_w = -\rho c_p\left(\frac{\nu}{Pr} + \frac{\nu_t}{Pr_t}\right)\frac{k_P^{1/2}}{\nu}\left.\frac{d\Theta}{dy^*}\right|_w = -\frac{\rho c_p k_P^{1/2}}{\mu}A_T, \tag{55}$$

whose resultant form is the same as Eq. (18) and can be calculated with A_T.

In the other cases (b)–(d), integration can be performed by the similar manner.

References

Ahmed, A., Demoulin, M., 2002. Turbulence modelling in the automotive industry. In: Rodi, W., Fueyo, N. (Eds.), Engineering Turbulence Modelling and Measurements, vol. 5. Elsevier Science Ltd., pp. 29–42.

Amano, R.S., 1984. Development of turbulence near wall model and its application to separated and reattached flows. Numer. Heat Transfer 7, 59–76.

Aupoix, B., Spalart, P.R., 2003. Extensions of the Spalart–Allmaras turbulence model to account for wall roughness. Int. J. Heat Fluid Flow 24, 454–462.

Cabot, W., Moin, P., 1999. Approximate wall boundary conditions in the large-eddy simulation of high Reynolds number flow. Flow Turb. Combust. 63, 269–291.

Cebeci, T., Bradshaw, P., 1977. Momentum Transfer in Boundary Layers. Hemisphere Publ. Co.

Chieng, C.C., Launder, B.E., 1980. On the calculation of turbulent heat transport downstream from an abrupt pipe expansion. Numer. Heat Transfer 3, 189–207.

Christoph, G.H., Pletcher, R.H., 1983. Prediction of rough-wall skin friction and heat transfer. AIAA J. 21, 509–515.

Ciofallo, M., Collins, W.M., 1989. k–ε predictions of heat transfer in turbulent re-circulating flows using an improved wall treatment. Numer. Heat Transfer 15, 21–47.

Craft, T.J., Launder, B.E., Suga, K., 1996. Development and application of a cubic eddy-viscosity model of turbulence. Int. J. Heat Fluid Flow 17, 108–115.

Craft, T.J., Iacovides, H., Yoon, J.H., 1999. Progress in the use of nonlinear two-equation models in the computation of convective heat-transfer in impinging and separating flows. Flow Turb. Combust. 63, 59–80.

Craft, T.J., Gerasimov, A.V., Iacovides, H., Launder, B.E., 2002. Progress in the generalization of wall-function treatments. Int. J. Heat Fluid Flow 23, 148–160.

Craft, T.J., Gant, S.E., Iacovides, H., Launder, B.E., 2004. A new wall function strategy for complex turbulent flows. Numer. Heat Transfer, Part B 45, 301–318.

Durbin, P.A., Medic, G., Seo, J.M., Eaton, J.K., Song, S., 2001. Rough wall modification of two-layer k–ε. ASME J. Fluids Eng. 123, 16–21.

Gerasimov, A.V., 2003. Development and validation of an analytical wall-function strategy for modelling forced, mixed and natural convection phenomena. Ph.D. Thesis. UMIST, Manchester, UK.

Grotjans, H., Menter, F.R., 1998. Wall functions for general application CFD codes. In: Papailiou, K.D. (Ed.), Computational Fluid, Dynamics 1998, ECCOMAS 98, Proc. Fourth European Computational Fluid Dynamics Conference. John Wiley & Sons Ltd., Chichester, UK, pp. 1112–1117.

Hanjalić, K., 2002. One-point closure models for buoyancy-driven turbulent flows. Annu. Rev. Fluid Mech. 34, 321–347.

Hosni, M.H., Coleman, H.W., Taylor, R.P., 1991. Measurements and calculations of rough-wall heat transfer in the turbulent boundary layer. Int. J. Heat Mass Transfer 34, 1067–1082.

Huang, P.G., Leschziner, M.A., 1983. An introduction and guide to the computer code TEAM. UMIST Mech. Eng. Rep., TF/83/9.

Iacovides, H., Raisee, M., 1999. Recent progress in the computation of flow and heat transfer in internal cooling passages of gas-turbine blades. Int. J. Heat Fluid Flow 20, 320–328.

Johnk, R.E., Hanratty, T.J., 1962. Temperature profiles for turbulent flow of air in a pipe. I. The fully developed heat-transfer region. Chem. Eng. Sci. 17, 867–879.

Johnson, R.W., Launder, B.E., 1982. Discussion of 'On the calculation of turbulent heat transport downstream from an abrupt pipe expansion'. Numer. Heat Transfer 5, 493–496.

Kays, W.M., Crawford, M.E., 1993. Convective Heat and Mass Transfer, third ed. McGraw-Hill, New York, pp. 298–301.

Krogstad, P.A., Antonia, R.A., Browne, L.W.B., 1992. Comparison between rough- and smooth-wall turbulent boundary layers. J. Fluid Mech. 245, 599–617.

Launder, B.E., 1984. Numerical computation of convective heat transfer in complex turbulent flows: time to abandon wall functions?. Int. J. Heat Mass Transfer 27, 1485–1490.

Launder, B.E., 1988. On the computation of convective heat transfer in complex turbulent flows. ASME J. Fluids Eng. 110, 1112–1128.

Launder, B.E., Sharma, B.I., 1974. Application of the energy-dissipation model of turbulence to the calculation of flow near a spinning disc. Lett. Heat Mass Transfer 1, 131–138.

Launder, B.E., Spalding, D.B., 1974. The numerical computation of turbulent flows. Comput. Meth. Appl. Mech. Eng. 3, 269–289.

Lien, F.S., Leschziner, M.A., 1994a. A general non-orthogonal finite-volume algorithm for turbulent flow at all speeds incorporating second-moment turbulence-transport closure. Part 1. Numerical Implementation. Comp. Meth. Appl. Mech. Eng. 114, 123–148.

Lien, F.S., Leschziner, M.A., 1994b. Upstream monotonic interpolation for scalar transport with application in complex turbulent flows. Int. J. Numer. Meth. Fluids 19, 527–548.

Moody, L.F., 1944. Friction factors for pipe flow. Trans. ASME 66, 671–678.

Nagano, Y., Hattori, H., Houra, T., 2004. DNS of velocity and thermal fields in turbulent channel flow with transverse-rib roughness. Int. J. Heat Fluid Flow 25, 393–403.

Nikuradse, J., 1933. Strömungsgesetze in rauhen rohren. VDI-Forschungsheft 361.

Patankar, S.V., 1980. Numerical heat transfer and fluid flow. Hemisphere/McGraw-Hill, Washington.

Patel, V.C., Yoon, J.Y., 1995. Application of turbulence models to separated flow over rough surfaces. ASME J. Fluids Eng. 117, 234–241.

Rhie, C.M., Chow, W.L., 1983. Numerical study of the turbulent flow past an airfoil with trailing edge separation. AIAA J. 21, 1525–1532.

Schlichting, H., 1979. Boundary-Layer Theory, seventh ed. McGraw-Hill, New York, pp. 615–626, 652–665.

Shih, T.-H., Povinelli, L.A., Liu, N.-S., 2003. Application of generalized wall function for complex turbulent flows. J. Turb. 4, 015.

Smith, B.R., 1990. The k–kl turbulence model and wall layer model for compressible flows. AIAA Paper 90–1483, June.

Song, S., Eaton, J.K., 2002. The effects of wall roughness on the separated flow over a smoothly contoured ramp. Exp. Fluids 33, 38–46.

Song, S., DeGraaff, D.B., Eaton, J.K., 2000. Experimental study of a separating, reattaching, and redeveloping flow over a smoothly contoured ramp. Int. J. Heat Fluid Flow 21, 512–519.

Tachie, M.F., Bergstrom, D.J., Balachandar, R., 2003. Roughness effects in low-Re_θ open-channel turbulent boundary layers. Exp. Fluids 35, 338–346.

Taylor, R.P., Coleman, H.W., Hodge, B.K., 1985. Prediction of turbulent rough-wall skin friction using a discrete element approach. ASME J. Fluids Eng. 107, 251–257.

Turner, A.B., Hubbe-Walker, S.E., Bayley, F.J., 2000. Fluid flow and heat transfer over straight and curved rough surfaces. Int. J. Heat Mass Transfer 43, 251–262.

van Mierlo, M.C.L.M., de Ruiter, J.C.C., 1988. Turbulence measurements above artificial dunes. Delft Hydraulics Lab. Rep., Q789, Delft, The Netherlands.